Rheology of capsule suspensions in plane Poiseuille flows

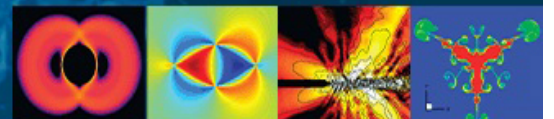**Huiyong Feng** (封慧勇), iD **Haibo Huang** (黄海波), **and** iD **Xi-Yun Lu** (陆夕云)

View Online   Export Citation   CrossMark

Physics of Fluids
GALLERY OF COVERS

Rheology of capsule suspensions in plane Poiseuille flows

View Online   Export Citation   CrossMark

Huiyong Feng (封慧勇), Haibo Huang (黄海波),[a] ID **and Xi-Yun Lu (陆夕云)** ID

AFFILIATIONS

Department of Modern Mechanics, University of Science and Technology of China, Hefei, Anhui 230026, China

Note: This paper is part of the Special Issue on the Lattice Boltzmann Method.
[a] Author to whom correspondence should be addressed: huanghb@ustc.edu.cn

ABSTRACT

The rheology of a capsule suspension in two-dimensional confined Poiseuille flow is studied numerically using an immersed-boundary lattice Boltzmann method. The effects of capsule volume fraction ϕ and bending stiffness E_b on the rheology of the suspension are investigated first. The apparent viscosity does not monotonically increase with ϕ: the variation curve can be divided into four flow regimes. In each regime, there is a distinct equilibrium spatial configuration. The overall lateral position of the capsules is directly connected with the apparent viscosity. Then, we propose to investigate the effect of inertia on the capsule configuration in dilute cases and the capsule transport in concentrated cases. For dilute cases, phase diagrams of flow regimes on the (ϕ, E_b) plane are plotted. It is found that, as the Reynolds number (Re) increases, the range of values for regime I, with a single-line configuration, reduces, while the range for regime II (transition configuration) increases. It is highly correlated with the equilibrium lateral position of a single capsule. For even larger Re, the range for regime IV (random configuration) increases rapidly and dominates because the larger inertia makes the arrangement more random. For concentrated cases, we observe that the optimal volume fraction, at which the transport of capsules is a maximum, increases with Re. This study may help to understand the collective behavior of capsules in Poiseuille flows.

Published under license by AIP Publishing. https://doi.org/10.1063/5.0032113

I. INTRODUCTION

Capsule suspensions are ubiquitous in both biological (blood) and industrial (mining and petroleum) systems. In the presence of capsules, Newtonian solvent fluids can exhibit non-Newtonian rheological properties. The rheological properties of the suspension are particularly interesting when different spatial configurations of capsules occur.[1,2]

The rheological properties of a capsule suspension are basically governed by the dynamics and lateral position of the capsule. The dynamics of a single capsule in Poiseuille flow has been extensively studied. It has been shown that with different bending stiffnesses, tube confinements, or viscosity ratios between the inner and outer fluid of the capsule membrane, the capsule can form parachute, bullet, and slipper shapes.[3–14] Thorough analyses of the entire phase diagram of these dynamical processes have been performed.[15–19] Lateral migration is another important physical quantity that needs to be considered. The variation of equilibrium lateral position with

the mechanical properties of a capsule has been studied.[20–24] It has been found that, in capsule suspensions, if the lateral positions of the capsules are close to the wall, the local viscosity in the vicinity of the walls, and therefore the apparent viscosity, is significantly enhanced.[25]

The connections between the suspension rheology and the lateral positions or spatial configuration of capsules have been discussed in the literature. Capsules in dilute or semi-dilute cases may be well-organized in one or two rows in simple shear flows or Poiseuille flows.[1,2,26–28] The spatial configuration depends on the fluid inertia, volume fraction, and mechanical properties of the capsules. Shen et al.[1] and Thiebaud et al.[2,29] studied the influence of spatial configurations on rheological suspension properties in simple shear flows. Krüger et al.[25] investigated the distribution and rheological properties of Poiseuille flows, but only at a specific volume fraction. In addition, most of the previous studies focused on the spatial configurations of rigid particles.[30–33] As far as we know, the variation of the spatial capsule configuration and

rheology with volume fraction has never been investigated for Poiseuille flows.

Most of the previous studies have focused on flows at very low Reynolds number.[1,2,25,34–38] However, the inertial effect also plays an important role in the distribution of capsules. It may be used to enhance mixing and it may also be applied to separate capsules in straight or curved geometry, according to their different equilibrium lateral positions. Some studies have systematically investigated the inertial effect on the dynamics of deformable objects.[39–50] However, most of these studies focused on the dynamics of a single capsule or the properties of capsule suspensions with a fixed volume fraction. In this study, the combined influence of fluid inertia and volume fraction on the spatial configurations of the capsule, as well as on the rheological properties of the fluid, is investigated.

Particle or capsule transportation in vessels or man-made pipes may be determined by the flow rate and the concentration of the suspension. Many studies have shown that there is an optimal concentration that maximizes material transfer in transport systems. For example, the optimal erythrocyte (red blood cell) volume fraction in humans is ~40%–50%.[1,51] In this paper, we explore the effect of fluid inertia on the optimal capsule volume fraction and explain it in the context of capsule shear stress.

In this study, we performed a series of numerical simulations to discuss the relation between capsule distributions and apparent viscosity in Poiseuille flows. The equilibrium spatial configurations are analyzed, and the overall lateral equilibrium location of capsules is quantified. Dilute and concentrated cases are discussed in detail. For dilute cases, phase diagrams of flow regimes on the (ϕ, E_b) plane are plotted and the inertial effect is analyzed. Capsules' distribution in the suspension is connected with the equilibrium lateral position of a single capsule. For concentrated cases, the inertial effect is also discussed. Besides, we observe an optimal volume fraction in which the capsules' flow rate is maximum. The influence of inertia on the optimal volume fraction is explored.

The article is organized as follows. In Sec. II, the membrane model and numerical method are introduced and the method is validated. Section III presents the main results for a single capsule and a capsule suspension. Finally, conclusions are provided in Sec. IV.

II. MEMBRANE MODEL AND NUMERICAL METHOD

A. Membrane model

The capsule is surrounded by a membrane, which prevents it from stretching, compressing, and bending excessively.[52] When the capsule deforms, to satisfy the non-slip boundary condition, there is a force jump across the membrane. The membrane then generates an elastic force $T(x, t)$ containing forces due to surface tension and bending. The surface tension force can be calculated from a constitutive law; here, the neo-Hookean law is employed. The surface tension is[53–55]

$$T_e = k_s(\epsilon - 1), \tag{1}$$

where k_s is the shear modulus of elasticity and ϵ is the stretch ratio. To include the bending resistance, the approach of Pozrikidis[54] is employed, which is

$$T_b = \frac{d}{dl}[k_b(\kappa - \kappa_0)], \tag{2}$$

where k_b is the bending modulus, l is the curve coordinate of the membrane, κ is the instantaneous curvature, and κ_0 is the reference curvature. The membrane elastic force is the sum of the two forces,

$$T = T_e t + T_b n, \tag{3}$$

where t and n are unit vectors in the tangent and normal directions, respectively.

B. Numerical method

Our numerical method combines the lattice Boltzmann method (LBM) and the immersed boundary method (IBM). The LBM originates from lattice gas automation (LGA). Macroscopically, it is able to solve the incompressible Navier–Stokes equations (see Ref. 56 for more details). The discretized lattice Boltzmann equation is

$$f_i(x + c_i\Delta t, t + \Delta t) - f_i(x,t) = \frac{1}{\tau}(f_i(x,t) - f_i^{eq}(x,t)) + \Delta tF_i, \tag{4}$$

where $f_i(x, t)$ is the discretized distribution function at location x and time t, $f_i^{eq}(x,t)$ is the equilibrium distribution function, c_i is the discretized velocity vector, and here the D2Q9 velocity model is adopted. τ is the relaxation time, and it is related to the kinematic viscosity v by $v = 1/2c_s^2\Delta t(2\tau - 1)$. F_i is the external force term.

The equilibrium distribution function is

$$f_i^{eq}(x,t) = \omega_i\rho\left[1 + \frac{1}{c_s^2}(c_i \cdot u) + \frac{1}{2c_s^4}(c_i \cdot u)^2 - \frac{1}{2c_s^2}(u \cdot u)\right]. \tag{5}$$

The external force term is written as[57]

$$F_i = \left(1 - \frac{1}{2\tau}\right)\omega_i\left(\frac{c_i - u}{c_s} + \frac{c_i \cdot u}{c_s^4}c_i\right) \cdot F, \tag{6}$$

where ω_i is the weighting factor. $\omega_i = 4/9$ for $i = 0$, $\omega_i = 1/9$ for $i = 1, 2, 3, 4$, and $\omega_i = 1/36$ for $i = 5, 6, 7, 8$. $c_s = \frac{1}{\sqrt{3}}\frac{\Delta x}{\Delta t}$ is the lattice sound speed, where Δx and Δt are lattice spacing and time step, respectively.

The macroscopic quantities can be obtained from the moments of the distribution function. The fluid density is

$$\rho = \sum f_i. \tag{7}$$

The fluid velocity is

$$\rho u = \sum c_i f_i + \frac{1}{2}\Delta tF. \tag{8}$$

The IBM was developed by Peskin[58] and is very useful for coupling the fluid flow and the movement of capsules. It has been applied extensively to fluid–structure interaction problems. It has also proved to be very useful for simulating the motion and deformation of capsules in fluid.[59] In this method, the solid body is immersed in the fluid and the membrane is discretized into many Lagrangian points. To ensure a non-slip boundary condition, the velocity of a Lagrangian point is interpolated from the surrounding fluid nodes, i.e.,

$$u(s) = \sum_f \delta(s - x) u(x), \tag{9}$$

where s and x are the locations of the Lagrangian points and fluid nodes, respectively, and δ is the delta function. The location of each Lagrangian point and the new geometry of the capsule at the next time step can be determined from the kinematic formula. Using Eq. (3), we can calculate the force acting on each Lagrangian point, which should be spread to surrounding fluid nodes, i.e.,

$$F(x) = \sum_m \delta(s - x) T(s). \tag{10}$$

It is noted that this force should be added to the lattice Boltzmann equation as an external force.[59] The delta function is chosen to be

$$\delta(x - s) = \frac{1}{\Delta x^2} \delta\left(\frac{x - x(s)}{\Delta x}\right) \delta\left(\frac{y - y(s)}{\Delta x}\right), \tag{11}$$

where

$$\delta(r) = \begin{cases} \frac{1}{4}\left(1 + \cos\left(\frac{\pi r}{2}\right)\right), & r \leq 2 \\ 0, & r > 2. \end{cases} \tag{12}$$

In this way, the physical non-slip boundary condition is satisfied.

C. Validation

To validate our numerical method, we simulate the motion of a capsule in a simple shear flow with shear rate $\dot{\gamma}$, as shown schematically in Fig. 1(a). A circular capsule is initially placed in the center of the computational domain. The radius of the capsule is a and the size of the computational domain is $16a \times 16a$. The Reynolds number is $Re = \frac{4\dot{\gamma}a^2}{\nu} = 0.05$, so the fluid inertia is very small. The capillary number is $Ca = (\rho\nu\dot{\gamma}a)/k_s = 0.04$ and the dimensionless bending moduli $E_b = k_b/(a^2 k_s)$ are 0.025, 0.05, and 0.1.

The Taylor deformation parameter $D_{xy} = \frac{L_{max} - L_{min}}{L_{max} + L_{min}}$ is usually used to quantify the capsule dynamics. A large D_{xy} denotes a large deformation. L_{max} and L_{min} are the major and minor axes of the capsule, respectively. Figure 1(b) shows D_{xy} as a function of time. It is seen that our results in the three different cases are all consistent with those in Ref. 60.
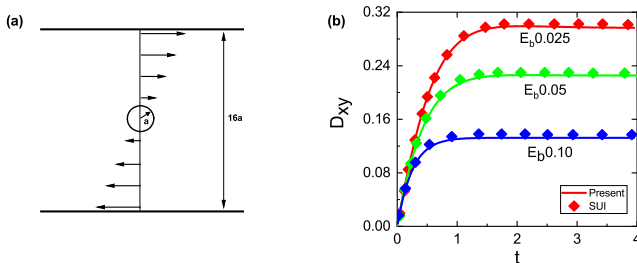
III. RESULTS AND DISCUSSION

In the present study, the suspension rheology in a channel of width h is investigated. Figure 2 shows a schematic of a capsule suspension in a two-dimensional (2D) Poiseuille flow. Periodic conditions are imposed at the inflow (left) and outflow (right) boundaries of the domain, as adopted by many previous studies.[25,36,55] Flow is induced by a body force g along the x-axis. The velocity profile of the unperturbed flow is

$$u_0 = \frac{gh^2}{2\mu_0}\left(\frac{y}{h} - \frac{y^2}{h^2}\right), \tag{13}$$

where μ_0 is the dynamic viscosity of the fluid.

In our simulations, the particle radius is $a = 25\Delta x$ and the membrane is discretized into 250 Lagrangian points so that the arc length is of the same order of magnitude as the lattice length. When the capsules get sufficiently close to each other, the high pressure between them would act as the repulsive force and push them away. In addition, because of deformation, the membranes of the capsule may contract inward. Hence, capsules do not overlap. In our simulations, no extra lubrication is included. For real blood flow, the diameters of human capillaries and arterioles are usually 3–55 times the cell radius.[34] Here, the channel width is $h = 6a$ and the channel length is $30a$, which is long enough to obtain accurate results.[55,61] The Reynolds number is defined as $Re = 2\rho Ua/\mu_0$, where U is the mean flow velocity. Other key parameters are the shear capillary number $Ca = \mu_0 U/k_s$, dimensionless bending modulus $E_b = k_b/(k_s a^2)$, and volume fraction $\phi = (N\pi a^2)/S$, where N is the number of capsules and S is the area of the computational domain. Here, Ca is set as a constant to 0.1 and the viscosity ratio between the internal and external fluids of the membrane is unity λ.

A. Dynamics of a single capsule

In this section, we present the behavior of a single capsule. In a Poiseuille flow, the shear rate changes from zero at the center of the channel to the peak value at the wall. The lateral locations of the capsules can significantly affect the suspension rheology. Here, we focus on the effects of Re and E_b on the lateral location of capsules.

The equilibrium lateral location y_e is normalized to $Y = |y_e - h/2|/(h/2)$. When $Y = 0$, the capsule is on the centerline of the channel. Figure 3(a) shows the equilibrium lateral position Y as a function of Re and E_b. It is found that when E_b is not very small, e.g., $E_b = 0.02$, Y first increases with Re and then decreases. The peak appears between $Re = 10$ and $Re = 30$. The increase or decrease depends mainly on two forces: the force toward the wall generated by the shear gradient and the force toward the centerline due to the effect of the wall. The behavior is the result of a competition between the two forces.[23]
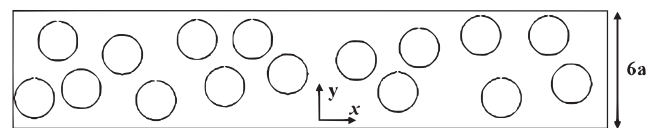

FIG. 1. (a) A capsule in a simple shear flow. (b) Evolution of the Taylor deformation parameter D_{xy}.

FIG. 2. Capsule suspension in a 2D Poiseuille flow. The capsules are randomly distributed initially.
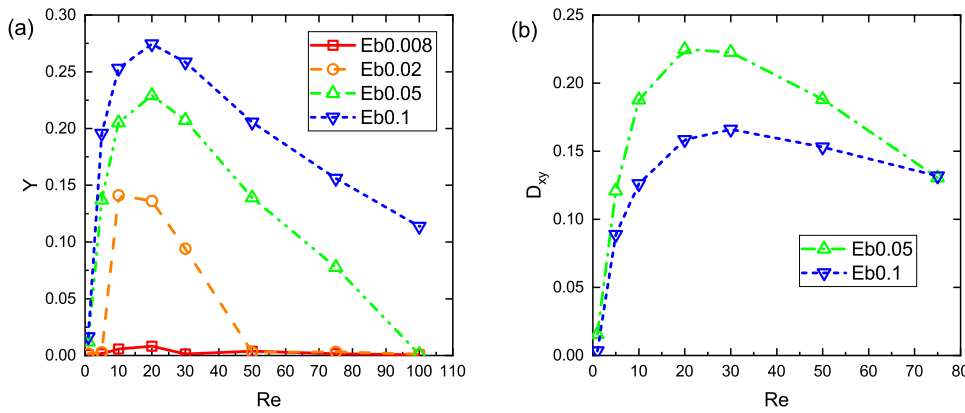
FIG. 3. (a) Equilibrium lateral location and (b) Taylor deformation of a single capsule as a function of Re and E_b.

It is also found that, for a given Re, the equilibrium state has softer capsules (smaller E_b) closer to the centerline. For example, at $Re = 20$, for $E_b = 0.1, 0.05, 0.02,$ and 0.008, the equilibrium lateral locations are $\sim 0.28, 0.23, 0.14,$ and 0.01, respectively. This trend is consistent with the conclusions of Krüger *et al.*[25] Here, we also note that when E_b is small enough, e.g., $E_b = 0.008$, the capsule almost remains at the centerline and its equilibrium lateral position is independent of Re.

Taylor deformation parameters of capsules are shown in Fig. 3(b). It can be found that capsules with larger E_b are less likely to deform. At a specific E_b, the variation trend of D_{xy} is similar to that of Y because at a larger Y, there is a larger local shear rate.

B. Apparent suspension viscosity and capsule distribution

In 2D Poiseuille flow without a capsule, the volume flux along the x-axis is

$$Q_0 = \int_0^h u_0(y)dy = \frac{gh^3}{12\mu_0}, \qquad (14)$$

where u_0 is the velocity along the x axis. For a capsule suspension, the formula for the volume flux Q_s is similar to Eq. (14) except μ_0 should be replaced by the apparent viscosity μ_a. Hence, if Q_s is known, the relative apparent viscosity μ_a can be obtained from[25,55]

$$\mu_a = \frac{\mu}{\mu_0} = \frac{Q_0}{Q_s}, \qquad (15)$$

where μ is the apparent viscosity of the capsule suspension.

Figure 4 shows the instantaneous μ_a for different volume fractions ϕ. It is found that after $t > 1000$ (t has been normalized by $L_y/2U$), each instantaneous μ_a curve varies around a constant value with a small amplitude. The change in the time-averaged value of apparent viscosity $\overline{\mu}_a$ is less than 1%, so we assume that the suspension flow has reached an equilibrium state in each case in Fig. 4.

The time-averaged apparent viscosity $\overline{\mu}_a$ quantifies a characteristic of the equilibrium state. Figure 5 shows $\overline{\mu}_a$ as a function of ϕ. We can see that, for a given E_b, $\overline{\mu}_a$ generally increases with ϕ. This can be understood as follows: as the number density of the capsules increases, the suspension flows less easily.

From Fig. 5, we can also see that $\overline{\mu}_a$ is usually smaller for softer capsules than for more rigid capsules, at a given ϕ. This is a well-known phenomenon in capsule suspensions.[62] Because the softer capsules adapt to the flow more easily, they do not disturb the flow field as much, so the apparent viscosity is closer to that of the solvent. The phenomenon can also be explained from the point of view of the capsule lateral position. It is presented later in this subsection.

Figure 5 shows that the apparent viscosity does not increase monotonically with ϕ. The curve can be divided into four sections according to the growth rate. In regime I ($\phi = 0\%-10\%$), $\overline{\mu}_a$ increases with ϕ. In regime II ($\phi = 10\%-18\%$), $\overline{\mu}_a$ increases slowly or even decreases with ϕ. In regime III ($\phi = 18\%-32\%$), $\overline{\mu}_a$ increases again until the next inflection point, which is around $\phi = 32\%$. In regime IV ($\phi > 32\%$), $\overline{\mu}_a$ increases rapidly with ϕ.

To understand the variation in apparent viscosity, we look at the typical equilibrium spatial configurations of the capsules in each flow regime, which are shown in Fig. 6. It is found that when ϕ is low (regime I), the capsules form a single-file configuration [see Fig. 6(I)] and are uniformly distributed.
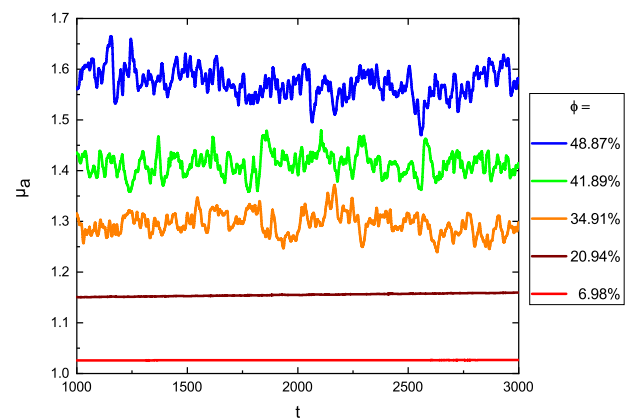

FIG. 4. Instantaneous apparent viscosity as a function of time in the cases with different ϕ but identical Re and E_b ($Re = 10$, $E_b = 0.008$). The curves from bottom to top are the cases with $\phi = 6.98\%, 20.94\%, 34.91\%, 41.89\%,$ and 48.87%, respectively.
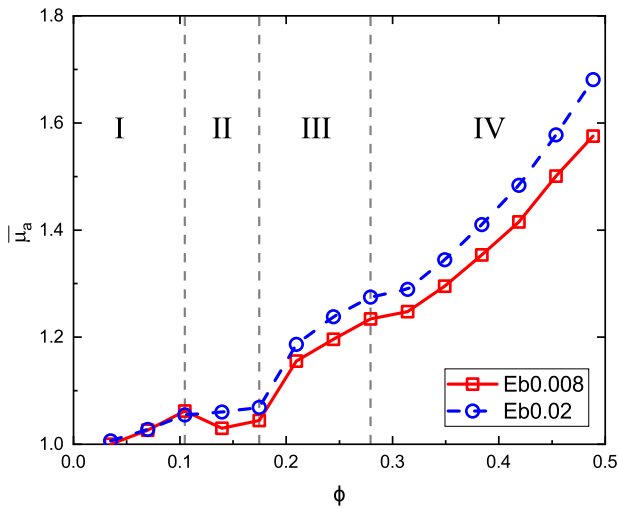
FIG. 5. Apparent viscosity as a function of ϕ at Re = 10. The curve can be divided into four regimes: regime I: ϕ = 0%–10%, regime II: ϕ = 10%–18%, regime III: ϕ = 18%–32%, and regime IV: ϕ > 32%. Vertical dashed lines denote borders of each regimes.

In regime II, it seems that the capsules no longer fit into one row, so a second row begins to develop [see Fig. 6(II)]. In this regime, ϕ is still not very large. The main feature is that the gap between capsules is large and two rows of capsules are arranged alternately. It should be noted that there is not always the same number of capsules on either side of the centerline. This is a transition state from a single-line to a double-line configuration. Figure 6(III) shows the typical double-line configuration of regime III. There are two rows, which are almost symmetric about the centerline. The number of capsules in each row is equal and the capsules do not shift between two rows. In regime IV, the suspension becomes denser with a larger ϕ. The capsules can shift between the two rows and the configuration becomes more random and unstable [see Fig. 6(IV)]. Interestingly, Shen *et al.*[1] also noticed similar phenomena in simple shear flows.

To describe the capsule distribution quantitatively, the equilibrium lateral position of the capsules and the depletion layer thickness of the suspension are discussed. The second moment of capsule density is defined to describe the overall lateral distribution,[25]

$$M_2 = \frac{1}{h} \int_0^h \phi(y)\left(y - \frac{h}{2}\right)^2 dy, \qquad (16)$$

where $\phi(y)$ is the volume fraction profile between the channel walls. For a given lateral position y, $\phi(y)$ is the ratio of the lattice nodes occupied by capsules to the total number of nodes, along the x direction. The normalized overall lateral position of the capsules is[25]

$$\Delta = \sqrt{\frac{4M_2}{\phi h^2}}. \qquad (17)$$

The larger the Δ is, the further the capsules are from the centerline. If the capsules spread homogeneously, $\Delta = 1/\sqrt{3} \approx 0.57$. The cell-free layer thickness d is defined as the minimum distance between the capsules and the walls. The variation in overall lateral position Δ as a function of ϕ is shown in Fig. 7(a): it is found that this variation is different in each regime.

It is found from Fig. 7(a) that when ϕ is small (regime I), Δ increases with increasing ϕ. Hence, in this regime, when the number of capsules increases, the capsules become further from the centerline [see Fig. 6(I)].

In regime II, the capsules do not concentrate in one row but are distributed over two rows [see Fig. 6(II)]. In this way, the number of capsules in each row may be lower than that in the single row in regime I. As mentioned above, fewer capsules in each row lead to a smaller overall lateral location of the row (Δ), so Δ in regime II may be smaller than in regime I [see Fig. 7(a)].

In regime III, as ϕ increases, there are more capsules in both rows, and the gap spacing between neighboring capsules becomes small [see Fig. 6(III)]. Due to the interaction between them, the capsules stay away from the centerline, so there is a jump in Δ between regimes II and III [see Fig. 7(a)].

In regime IV, the two-line configuration becomes unstable and some capsules are squeezed into the gap between the two rows, i.e., the centerline region. Hence, the overall lateral location decreases and there is a drop in Δ between regimes III and IV. When the number of capsules further increases, extra capsules are squeezed to the region close to the wall, so the overall Δ increases with increasing ϕ in regime IV [see Fig. 7(a)]. Hence, the overall lateral displacement is highly correlated with the apparent viscosity. When the capsules are closer to the wall, due to high viscosity dissipation, the apparent viscosity of the suspension increases.[25]
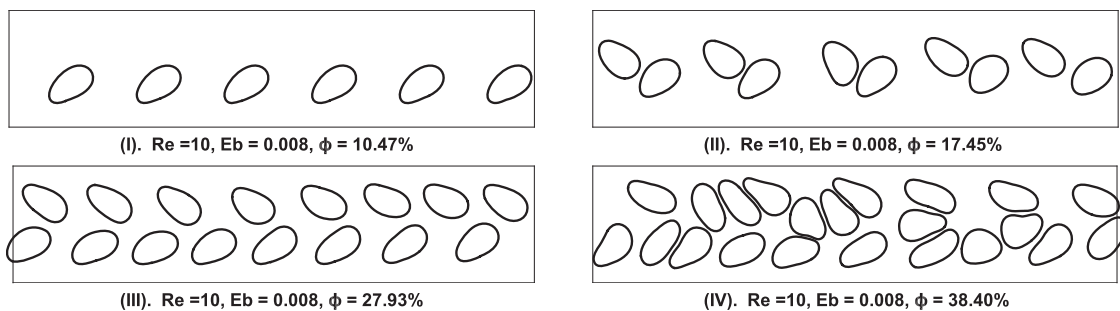

(I). Re =10, Eb = 0.008, ϕ = 10.47%

(II). Re =10, Eb = 0.008, ϕ = 17.45%

(III). Re =10, Eb = 0.008, ϕ = 27.93%

(IV). Re =10, Eb = 0.008, ϕ = 38.40%

FIG. 6. Equilibrium configurations in regimes I–IV: (I) the one-file configuration, (II) the transition configuration, (III) the two-file configuration, and (IV) the random configuration.
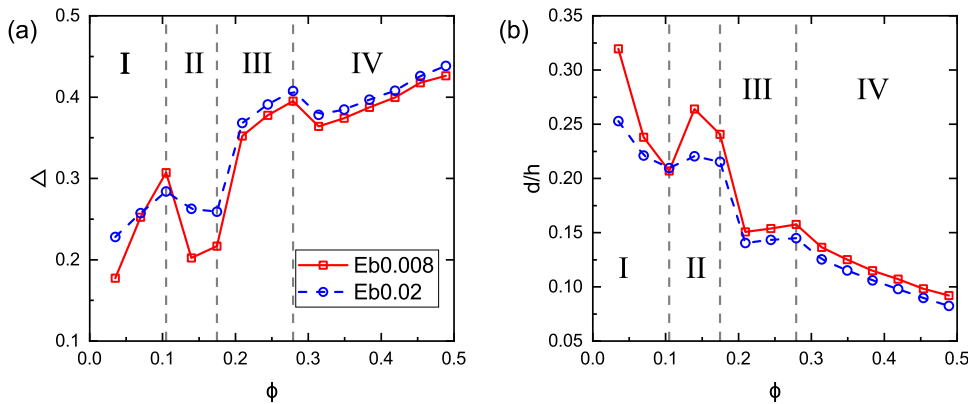
FIG. 7. (a) Equilibrium lateral position of capsules and (b) equilibrium depletion layer thickness of the capsule suspension at $Re = 10$ and $E_b = 0.008, 0.02$. Δ and d are averaged over a long time. Vertical dashed lines denote borders of the regimes.

In the following, we discuss the effect of the bending rigidity of the capsules. In Fig. 7(a), the curve for $E_b = 0.02$ is mostly above the curve for $E_b = 0.008$, so Δ tends to be larger for rigid capsules than for soft capsules. This means that more rigid capsules are closer to the wall, leading to a larger $\bar{\mu}_a$. In Fig. 7(a), at $\phi \approx 10\%$, there is an exception that Δ for $E_b = 0.008$ is larger than that for $E_b = 0.02$. In fact, this exception can be attributed to the configuration transition. The configurations of cases $E_b = 0.008$ and $E_b = 0.02$ at $\phi \approx 10\%$ are single-line and transition states, respectively. According to the analysis above, the transition state is closer to the centerline (smaller Δ).

Figure 7(b) shows the depletion layer thickness d as a function of ϕ. d is approximately complementary to Δ: when Δ increases, the capsules come closer to the wall and d decreases. Hence, the depletion layer thickness generally decreases with increasing ϕ.

Figure 8 shows $\phi(y)$ for four typical cases belonging to regimes I to IV. For $\phi = 10.47\%$, this corresponds to regime I with the single-line configuration. The curve is asymmetric because the capsules deviate from the centerline and concentrate on one side. For the case $\phi = 13.96\%$, this corresponds to regime II with the transition configuration. It seems that both rows of capsules are concentrated closer to the centerline. For the cases $\phi = 27.93\%$ and 31.42%, these correspond to regime III and IV (the random configuration), respectively. In the random configuration, more capsules appear in the centerline region than in the two-file configuration (see the blue dashed-dotted line and black dotted line). Hence, the overall lateral location (Δ) decreases when ϕ goes from 27.93% to 31.42%. These observations are consistent with the above analysis of Fig. 7.

In summary, the configuration of capsules is directly correlated with the overall equilibrium lateral location, which determines the apparent viscosity of the suspension.

C. Dilute cases

The following discussions are based on dilute and concentrate cases. The dilute cases include the cases in regimes I, II, and III. Their volume fraction is usually less than 25%, which may depend on Re. The concentrated cases are in regime IV with $\phi > 25\%$. For dilute cases, the phase diagrams of the regimes and the Reynolds number

effect on the phase diagrams would be discussed. For concentrate cases, the capsule flow rate is investigated.

In this subsection, we discuss the dilute cases. The E_b–ϕ phase diagrams of configurations at different Re are shown in Fig. 9. As expected, in all three phase diagrams, regime I mainly appears in low ϕ regions while regime IV appears when ϕ is large. The differences between the phase diagrams are analyzed in the following.

From Fig. 9(a), it is found that, at $Re = 1$, regime I is dominant and it occupies about half of the (ϕ, E_b) plane. At $Re = 10$, the area of regime II is larger and it is the major regime, especially for large E_b. This can be attributed to the equilibrium lateral position of a single capsule. At $Re = 1$, there is only one equilibrium lateral position, on the centerline. Under these circumstances, capsules tend to move toward the centerline rather than spread out on either side of the centerline until the single row is saturated (see Fig. 10). Conversely, at $Re = 10$, the equilibrium lateral position of a single
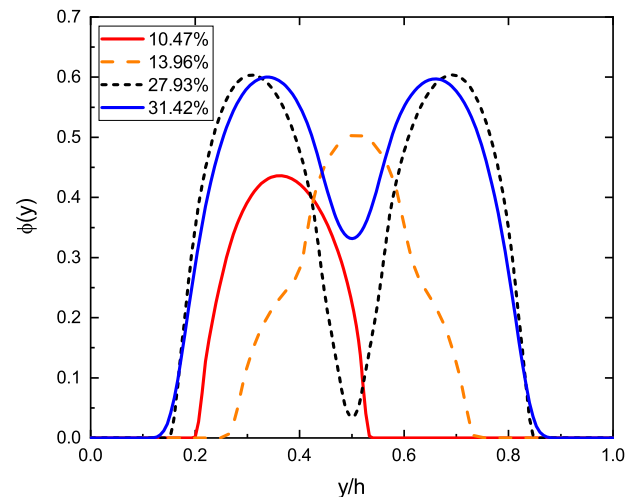

FIG. 8. Volume distribution along the y axis of different volume fractions at $Re = 10$ and $E_b = 0.008$. Red line: $\phi = 10.47\%$, orange dashed line: $\phi = 13.96\%$, black dotted line: $\phi = 27.93\%$, and blue dashed-dotted line: $\phi = 31.24\%$.
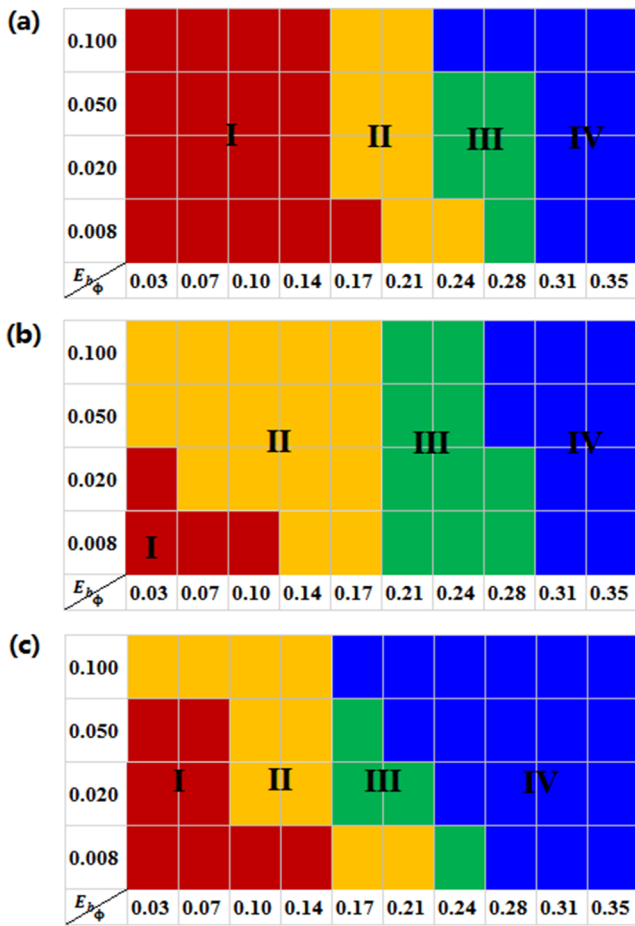
FIG. 9. Phase diagrams in the (ϕ, E_b) plane for (a) Re = 1, (b) Re = 10, and (c) Re = 50.

tends to be random. In this way, regime IV dominates the phase diagram. On the other hand, Fig. 9(c) also shows that the area of regime I increases slightly at Re = 50 compared to that at Re = 10. To understand this, we check the equilibrium lateral position of a single capsule in Fig. 3 and find that, in the case of Re = 50, the capsule is closer to the centerline than in the case of Re = 10, especially at small E_b, e.g., when E_b = 0.008 and 0.02, the capsule is on the centerline. Just like the situation at Re = 1, capsules tend to stay on the centerline until the row becomes saturated at Re = 50, so the range of regime I increases slightly again.

It is noticed that in Figs. 9(b) and 9(c), when ϕ is small and E_b is large, a part of regime II plotted may become regime I, which depends on the initial capsule distributions. If all capsules are initially located on one side of the centerline, it would form the equilibrium one-file configuration (regime I). Otherwise, the transition structure (regime II) would appear. Since the capsules initially located on both sides of the centerline is more general, in Figs. 9(b) and 9(c), the region (small ϕ and larger E_b) is still labeled regime II.

Channel width h is another important parameter that would influence the regime transitions. The (ϕ, h) phase diagram is shown in Fig. 11(a). It is found that when $h = 4a$, the channel confinement is so strong that only regime I would appear and no matter how we change the E_b, there only is regime I in a dilute suspension. As h increases, e.g., $h = 6a$, regimes II, III, and IV appear. When the channel is wide, e.g., $h = 8a$, only regimes III and IV appear even in a very dilute suspension. Because the confinement effect of the channel is diminished, the capsules can move more freely and they do not necessarily stay in just a single row or two rows. Figure 11(b) shows the (ϕ, E_b) phase diagram at $h = 8a$. Regime IV expands with the increase in E_b and the variation trend is the same as that at $h = 6a$ (see Fig. 9). Hence, $h = 6a$ is a typical channel in which all the regime transitions will happen at different E_b and Re.

In summary, the capsule configuration depends not only on the inertia and mechanical modulus but also on the channel width and the equilibrium lateral position of a single capsule.

D. Concentrated cases

In this subsection, the apparent viscosity and capsule flow rate for high volume fractions (ϕ > 25%) are studied. Under these circumstances, the capsules generally migrate randomly (regime IV).

To investigate the effect of inertia, we study the behavior of a suspension with a fixed volume fraction at different Re. Figure 12 shows $\bar{\mu}_a$ as a function of Re and E_b when Re < 80. It is found that when E_b = 0.05, $\bar{\mu}_a$ increases monotonically with increasing Re. However, when E_b is smaller, $\bar{\mu}_a$ increases first and then decreases with increasing Re. This result is consistent with that of Ref. 25.

The equilibrium lateral position and depletion layer thickness are plotted as a function of Re in Fig. 13. The variation in the equilibrium lateral position is similar to that of apparent viscosity (Fig. 12), since these two quantities are strongly correlated. It seems that the capsules are strongly focused toward the centerline upon increasing Re: this is referred to as "inertial focusing."

capsule is off-center; the capsule can reach equilibrium on either side of the centerline. Capsules reach equilibrium on both sides rather than only one side of the centerline, even if the single row is not saturated. The transition configuration forms easily [Fig. 6(b)] at Re = 10. Therefore, the range of ϕ values for regime I is relatively small and regime II dominates at Re = 10.

With increasing inertia, the borders of regimes III and IV move toward the left, especially for rigid capsules, at Re = 50. It can be seen from Fig. 9(c) that, compared to Re = 1 and 10, the inertia at Re = 50 is so large that even at low ϕ the distribution of capsules
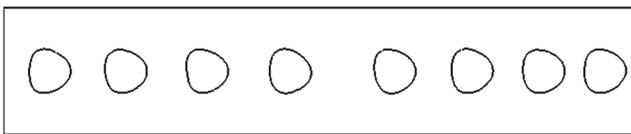

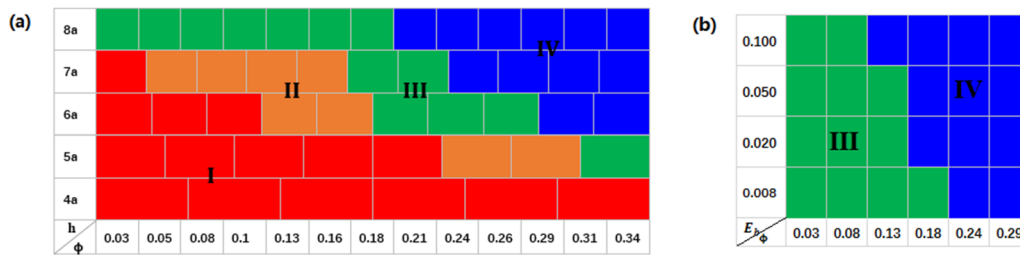**FIG. 10**. One-file configuration along the centerline.

FIG. 11. (a) Phase diagram in the (ϕ, h) plane for the cases of Re = 10 and E_b = 0.008 and (b) phase diagram in the (ϕ, E_b) plane for the cases of Re = 10 and h = 8a.

The connections between Figs. 12 and 13 can be understood in the following way. First, we recall the variation of the lateral location for a single capsule (see Fig. 3). It increases first and then decreases with increasing Re; the overall trend is similar to that of a capsule suspension. Moreover, the range of Re where the maximum lateral equilibrium position of a single capsule appears is between Re = 10 and 30. This coincides with the range for the capsule suspension, which is between Re = 20 and 40. Since the dense capsule suspension is composed of many capsules, there is a natural connection between the behavior of many capsules and that of a single capsule. For example, if a single capsule migrates close to the wall, it is impossible for a group of such capsules to stay away from the wall. On the other hand, the distribution of capsules in the suspension is significantly affected by the interactions between capsules. As can be seen, in a dense suspension at a larger Re, the overall equilibrium lateral location is still large and not as close to zero as that in the case of a single capsule. It is easy to imagine that the dispersion of the capsules is caused by the interactions between the capsules.
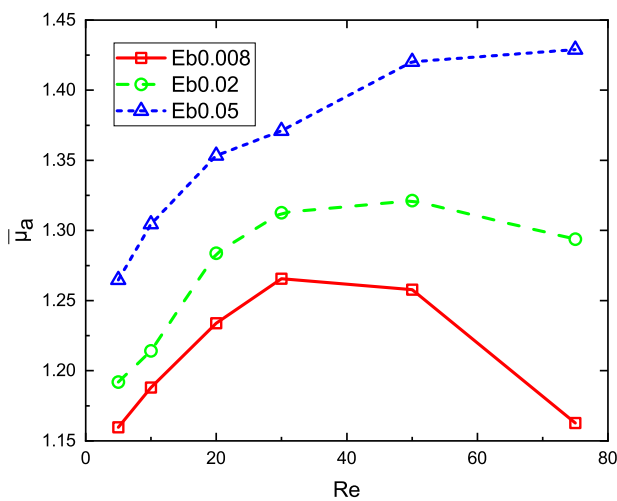
The capsule flow rate Q_c is another important issue. It is defined by determining the capsule area through a given cross section of the channel in unit time and is normalized by the flow rate of the capsule-free fluid Q_0. According to Ref. 34, there is a maximum capsule flow rate (or optimal transport) at an optimal value of ϕ. The optimal transport appears between ϕ = 30% and ϕ = 50% in their simulations. Our results for normalized capsule flow rates $\frac{Q_c}{Q_0}$ at Re = 1.0, 10, and 20 are shown in Fig. 14(a). It is found that there is an optimal transport at ϕ = 35%–45%, which is consistent with their result. In addition, the optimal volume fraction increases from 0.35 to about 0.45 with increasing Re. It is noted that the capsule flow rate Q_c increases with increasing Re. However, because Q_0 increases more significantly with increasing Re, the normalized capsule flow rate decreases with increasing Re.

The flow rate of a fluid usually depends on its viscosity. It is worth investigating how the viscosity of the suspension affects the transport of capsules. To do this, we analyze the capsule shear stress. The particle stress tensor $\sum_{ij}$ can be obtained from[62,63]

$$\sum_{ij} = \frac{1}{V\phi} \sum_{1}^{N} \int \left[f_i x_i' + \mu_0 (\lambda - 1)(u_i n_j + u_j n_i) \right] dA, \quad (18)$$

where f_i is the elastic force in the membrane, $\boldsymbol{x}'$ and $\boldsymbol{u}$ are the position and velocity on the capsule surface, respectively, $\boldsymbol{n}$ is the unit vector normal to the capsule surface, V is the volume of the domain and N is the number of capsules. The capsule shear stress is

$$S_{xy} = \frac{\sum_{12}}{\mu_0 \dot{\gamma}}, \quad (19)$$

where $\dot{\gamma}$ is defined as $2U/L_y$. Capsule shear stress as a function of ϕ is plotted in Fig. 14(b). It is found that the capsule shear stress reaches a minimum at ϕ = 38%, 42%, and 45% for Re = 1.0, 10, and 20, respectively. At these volume fractions, the capsule flow rates reach their maxima [see Fig. 14(a)]. Hence, the capsule shear stress is highly correlated with the transport of capsules. The capsule shear stress is analogous to the drag force on the capsule exerted by the surrounding fluid. A small drag force promotes the movement of capsules, which leads to a large capsule flow rate.
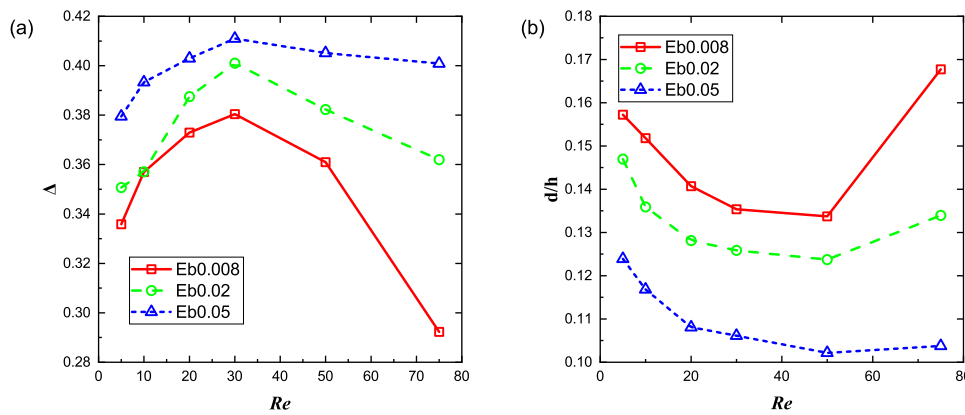

FIG. 12. Apparent viscosity $\overline{\mu}_a$ as a function of Re (ϕ is around 26.18%).

FIG. 13. Lateral position (a) and depletion layer thickness (b) as functions of *Re*.
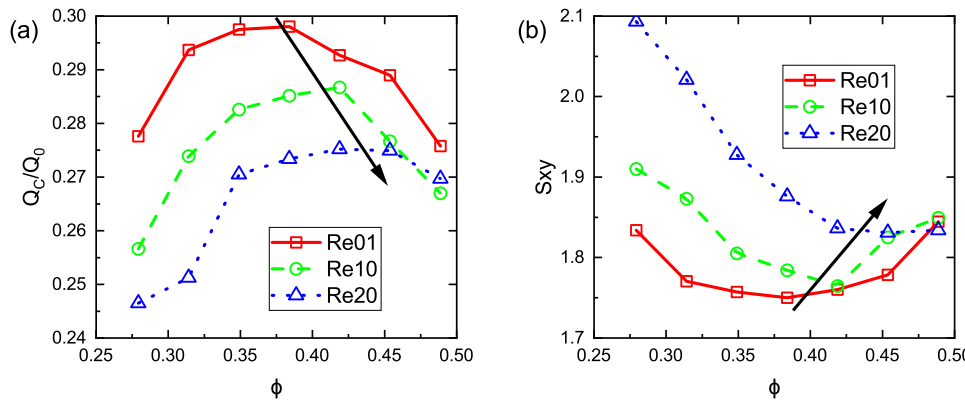

FIG. 14. Capsule flow rate (a) and capsule shear stress (b) as functions of ϕ. The solid arrows approximately link the peaks or valleys from low *Re* to high *Re* cases.

IV. CONCLUSION

In this study, we performed 2D simulations of capsule suspensions using the immersed-boundary and lattice-Boltzmann methods. We found that the increase in apparent viscosity with volume fraction is non-monotonic and can be divided into four regimes. In each regime, capsules exhibit distinct configurations: single line, transition, double line, and random. To analyze the configurations quantitatively, the overall lateral location (Δ), depletion layer thickness (d), and volume distribution [$\phi(y)$] are presented. It is found that capsule configurations affect the equilibrium Δ and they are highly correlated with the apparent viscosity of the suspension.

Typical dilute cases (capsules are well-organized, $\phi < 25\%$) and dense cases (capsules are random, $\phi > 25\%$) are discussed. In dilute cases, the phase diagram in the (ϕ, E_b) plane is plotted and the inertial effect is investigated. When *Re* is small (*Re* = 1), regime I dominates the phase diagram. As *Re* increases (*Re* = 10), regime I decreases and regime II expands. This is due to the equilibrium lateral position of a single capsule. At *Re* = 1, the equilibrium position is on the centerline. With the increase in ϕ, the capsules can only stay on the single row (centerline) until the row is saturated. Thus, regime I can occupy a large area of the phase diagram. However,

for *Re* = 10, there are two equilibrium lateral positions. Capsules would stay on both sides rather than one side of the centerline, so it is easy to form regime II. At a larger *Re* (*Re* = 50), regime IV (random configuration) occupies about half of the (ϕ, E_b) plane because larger inertia makes the arrangement more random. Besides, at *Re* = 50, regime I also increases slightly compared to that of *Re* = 10 since, for a single capsule, the equilibrium position is on the centerline at *Re* = 50. In summary, the capsule configuration is determined by not only the inertia and mechanical modulus but also the channel width and the equilibrium lateral position of a single capsule.

In dense cases, inertia focusing is observed. Again, we found that the overall behavior of the capsule suspension depends on not only the dynamics of a single capsule but also the capsule–capsule interaction, which is consistent with Ref. 25. Then, the capsule flow rate as a function of ϕ is studied at different *Re*. Optimal transport is observed at $\phi = 35\%$–45% with the smallest capsule shear stress. In fact, the capsule shear stress is the analogy to the drag force. A smaller capsule shear stress, i.e., a smaller drag force, would lead to a larger capsule flow rate. In addition, the optimal volume fraction increases with the increase in *Re*. This study may shed some light on understanding the collective behavior of capsules in Poiseuille flows.

DATA AVAILABILITY

The data that support the findings of this study are available from the corresponding author upon reasonable request.

REFERENCES

[1]Z. Shen, A. Farutin, M. Thiébaud, and C. Misbah, "Interaction and rheology of vesicle suspensions in confined shear flow," Phys. Rev. Fluids **2**, 103101 (2017).

[2]M. Thiebaud, Z. Shen, J. Harting, and C. Misbah, "Prediction of anomalous blood viscosity in confined shear flow," Phys. Rev. Lett. **112**, 238304 (2014).

[3]R. Rivera, X. Zhang, and M. D. Graham, "Mechanistic theory of margination and flow-induced segregation in confined multicomponent suspensions: Simple shear and Poiseuille flows," Phys. Rev. Fluids **1**, 060501 (2016).

[4]G. Coupier, B. Kaoui, T. Podgorski, and C. Misbah, "Noninertial lateral migration of vesicles in bounded Poiseuille flow," Phys. Fluids **20**, 1 (2008).

[5]G. Coupier, A. Farutin, C. Minetti, T. Podgorski, and C. Misbah, "Shape diagram of vesicles in Poiseuille flow," Phys. Rev. Lett. **108**, 178106 (2012).

[6]C. Pozrikidis, "Numerical simulation of cell motion in tube flow," Ann. Biomed. Eng. **33**, 165 (2005).

[7]G. Ma, J. S. Hua, and H. Li, "Numerical modeling of the behavior of an elastic capsule in a microchannel flow: The initial motion," Phys. Rev. E **79**, 046710 (2009).

[8]H. Li and G. Ma, "Modeling performance of a two-dimensional capsule in a microchannel flow: Long-term lateral migration," Phys. Rev. E **82**, 026304 (2010).

[9]W. Xiong and J. Zhang, "Shear stress variation induced by red blood cell motion in microvessel," Ann. Biomed. Eng. **38**, 2649 (2010).

[10]L. L. Shi, Y. Yu, T. W. Pan, and R. Glowinski, "Oscillating motions of neutrally buoyant particle and red blood cell in Poiseuille flow in a narrow channel," Phys. Fluids **26**, 041904 (2014).

[11]X.-Q. Hu, A.-V. Salsac, and D. Barthès-Biesel, "Flow of a spherical capsule in a pore with circular or square cross-section," J. Fluid Mech. **705**, 176 (2011).

[12]T. Ye, H. X. Shi, L. N. Peng, and Y. Li, "Numerical studies of a red blood cell in rectangular microchannels," J. Appl. Phys. **122**, 084701 (2017).

[13]J. M. Barakat and E. S. G. Shaqfeh, "Stokes flow of vesicles in a circular tube," J. Fluid Mech. **851**, 606 (2018).

[14]X. Zhang and M. D. Graham, "Multiplicity of stable orbits for deformable prolate capsules in shear flow," Phys. Rev. Fluids **5**, 023603 (2020).

[15]N. Tahiri, T. Biben, H. Ez-Zahraouy, A. Benyoussef, and C. Misbah, "On the problem of slipper shapes of red blood cells in the microvasculature," Microvasc. Res. **85**, 40 (2013).

[16]Z. Boujja, C. Misbah, H. Ez-Zahraouy, A. Benyoussef, T. John, C. Wagner, and M. M. Muller, "Vesicle dynamics in confined steady and harmonically modulated Poiseuille flows," Phys. Rev. E **98**, 043111 (2018).

[17]Y. Oya and T. Kawakatsu, "Onsager's variational principle for the dynamics of a vesicle in a Poiseuille flow," J. Chem. Phys. **148**, 114905 (2018).

[18]B. Kaoui, N. Tahiri, T. Biben, H. Ez-Zahraouy, A. Benyoussef, G. Biros, and C. Misbah, "Complexity of vesicle microcirculation," Phys. Rev. E **84**, 041906 (2011).

[19]D. A. Fedosov, M. Peltomäki, and G. Gompper, "Deformation and dynamics of red blood cells in flow through cylindrical microchannels," Soft Matter **10**, 4258 (2014).

[20]D. Alghalibi, M. E. Rosti, and L. Brandt, "Inertial migration of a deformable particle in pipe flow," Phys. Rev. Fluids **4**, 104201 (2019).

[21]B. Kaoui, G. H. Ristow, I. Cantat, C. Misbah, and W. Zimmermann, "Lateral migration of a two-dimensional vesicle in unbounded Poiseuille flow," Phys. Rev. E **77**, 021903 (2008).

[22]J. Zhang, "Effect of suspending viscosity on red blood cell dynamics and blood flows in microvessels," Microcirculation **18**, 562 (2011).

[23]L. L. Shi, T. W. Pan, and R. Glowinski, "Lateral migration and equilibrium shape and position of a single red blood cell in bounded Poiseuille flows," Phys. Rev. E **86**, 056308 (2012).

[24]S. Nix, Y. Imai, D. Matsunaga, T. Yamaguchi, and T. Ishikawa, "Lateral migration of a spherical capsule near a plane wall in Stokes flow," Phys. Rev. E **90**, 043009 (2014).

[25]T. Krüger, B. Kaoui, and J. Harting, "Interplay of inertia and deformability on rheological properties of a suspension of capsules," J. Fluid Mech. **751**, 725 (2014).

[26]K. J. Humphry, P. M. Kulkarni, D. A. Weitz, J. F. Morris, and H. A. Stone, "Axial and lateral particle ordering in finite Reynolds number channel flows," Phys. Fluids **22**, 081703 (2010).

[27]G. R. Lazaro, A. Hernandez-Machado, and I. Pagonabarraga, "Collective behavior of red blood cells in confined channels," Eur. Phys. J. E **42**, 46 (2019).

[28]A. Nait-Ouhra, A. Farutin, H. Ez-Zahraouy, A. Benyoussef, and C. Misbah, "Rheology of a confined vesicle suspension," Phys. Rev. Fluids **4**, 103602 (2019).

[29]A. Nait Ouhra, A. Farutin, O. Aouane, H. Ez-Zahraouy, A. Benyoussef, and C. Misbah, "Shear thinning and shear thickening of a confined suspension of vesicles," Phys. Rev. E **97**, 012404 (2018).

[30]Z. Pan, R. Zhang, C. Yuan, and H. Wu, "Direct measurement of microscale flow structures induced by inertial focusing of single particle and particle trains in a confined microchannel," Phys. Fluids **30**, 102005 (2018).

[31]X. Hu, J. Lin, and X. Ku, "Inertial migration of circular particles in Poiseuille flow of a power-law fluid," Phys. Fluids **31**, 073306 (2019).

[32]W. Liu and C. Wu, "Analysis of inertial migration of neutrally buoyant particle suspensions in a planar Poiseuille flow with a coupled lattice Boltzmann method-discrete element method," Phys. Fluids **31**, 063301 (2019).

[33]S. Kahkeshani, H. Haddadi, and D. D. Carlo, "Preferred interparticle spacing in trains of particles in inertial microchannel flows," J. Fluid Mech. **786**, R3 (2015).

[34]A. Farutin, Z. Y. Shen, G. Prado, V. Audemar, H. Ez-Zahraouy, A. Benyoussef, B. Polack, J. Harting, P. M. Vlahovska, T. Podgorski, G. Coupier, and C. Misbah, "Optimal cell transport in straight channels and networks," Phys. Rev. Fluids **3**, 103603 (2018).

[35]N. Takeishi, M. E. Rosti, Y. Imai, S. Wada, and L. Brandt, "Haemorheology in dilute, semi-dilute and dense suspensions of red blood cells," J. Fluid Mech. **872**, 818 (2019).

[36]S. K. Doddi and P. Bagchi, "Three-dimensional computational modeling of multiple deformable cells flowing in microvessels," Phys. Rev. E **79**, 046318 (2009).

[37]J. R. Clausen, D. A. Reasor, and C. K. Aidun, "The rheology and microstructure of concentrated non-colloidal suspensions of deformable capsules," J. Fluid Mech. **685**, 202 (2011).

[38]H. Zhao and E. S. G. Shaqfeh, "The dynamics of a non-dilute vesicle suspension in a simple shear flow," J. Fluid Mech. **725**, 709 (2013).

[39]J. T. Ma, L. C. Xu, F. B. Tian, J. Young, and J. C. S. Lai, "Dynamic characteristics of a deformable capsule in a simple shear flow," Phys. Rev. E **99**, 023101 (2019).

[40]S. K. Doddi and P. Bagchi, "Effect of inertia on the hydrodynamic interaction between two liquid capsules in simple shear flow," Int. J. Multiphase Flow **34**, 375 (2008).

[41]A. Kilimnik, W. Mao, and A. Alexeev, "Inertial migration of deformable capsules in channel flow," Phys. Fluids **23**, 123302 (2011).

[42]A. Nourbakhsh, S. Mortazavi, and Y. Afshar, "Three-dimensional numerical simulation of drops suspended in Poiseuille flow at non-zero Reynolds numbers," Phys. Fluids **23**, 123303 (2011).

[43]S. J. Shin and H. J. Sung, "Inertial migration of an elastic capsule in a Poiseuille flow," Phys. Rev. E **83**, 046321 (2011).

[44]Y. Kim and M. C. Lai, "Numerical study of viscosity and inertial effects on tank-treading and tumbling motions of vesicles under shear flow," Phys. Rev. E **86**, 066321 (2012).

[45]A. Laadhari, P. Saramito, and C. Misbah, "Vesicle tumbling inhibited by inertia," Phys. Fluids **24**, 031901 (2012).

[46]D. Salac and M. J. Miksis, "Reynolds number effects on lipid vesicles," J. Fluid Mech. **711**, 122 (2012).

[47] S. J. Shin and H. J. Sung, "Dynamics of an elastic capsule in moderate Reynolds number Poiseuille flow," Int. J. Heat Fluid Flow **36**, 167 (2012).

[48] Z. Y. Luo, S. Q. Wang, L. He, F. Xu, and B. F. Bai, "Inertia-dependent dynamics of three-dimensional vesicles and red blood cells in shear flow," Soft Matter **9**, 9651 (2013).

[49] Y.-L. Chen, "Inertia- and deformation-driven migration of a soft particle in confined shear and Poiseuille flow," RSC Adv. **4**, 17908 (2014).

[50] L. Shi, T. W. Pan, and R. Glowinski, "Deformation of a single red blood cell in bounded Poiseuille flows," Phys. Rev. E **85**, 016307 (2012).

[51] K. H. Jensen, W. Kim, N. M. Holbrook, and J. W. M. Bush, "Optimal concentrations in transport systems," J. R. Soc., Interface **10**, 20130138 (2013).

[52] P. M. Vlahovska, T. Podgorski, and C. Misbah, "Vesicles and red blood cells in flow: From individual dynamics to rheology," C. R. Phys. **10**, 775 (2009).

[53] P. Bagchi, P. C. Johnson, and A. S. Popel, "Computational fluid dynamic simulation of aggregation of deformable cells in a shear flow," J. Biomech. Eng. **127**, 1070 (2005).

[54] C. Pozrikidis, "Effect of membrane bending stiffness on the deformation of capsules in simple shear flow," J. Fluid Mech. **440**, 269 (2001).

[55] J. Zhang, P. C. Johnson, and A. S. Popel, "An immersed boundary lattice Boltzmann approach to simulate deformable liquid capsules and its application to microscopic blood flows," Phys. Biol. **4**, 285 (2007).

[56] S. Chen and G. D. Doolen, "Lattice Boltzmann method for fluid flows," Annu. Rev. Fluid Mech. **30**, 329 (1998).

[57] Z. L. Guo, C. G. Zheng, and B. C. Shi, "Discrete lattice effects on the forcing term in the lattice Boltzmann method," Phys. Rev. E **65**, 046308 (2002).

[58] C. S. Peskin, "The immersed boundary method," Acta Numer. **11**, 479 (2002).

[59] Z.-G. Feng and E. E. Michaelides, "The immersed boundary-lattice Boltzmann method for solving fluid-particles interaction problems," J. Comput. Phys. **195**, 602 (2004).

[60] Y. Sui, Y. T. Chew, P. Roy, X. B. Chen, and H. T. Low, "Transient deformation of elastic capsules in shear flow: Effect of membrane bending stiffness," Phys. Rev. E **75**, 066301 (2007).

[61] A. Lamura and G. Gompper, "Dynamics and rheology of vesicle suspensions in wall-bounded shear flow," Europhys. Lett. **102**, 28004 (2013).

[62] P. Bagchi and R. M. Kalluri, "Rheology of a dilute suspension of liquid-filled elastic capsules," Phys. Rev. E **81**, 056320 (2010).

[63] M. Thiebaud and C. Misbah, "Rheology of a vesicle suspension with finite concentration: A numerical study," Phys. Rev. E **88**, 062707 (2013).